www.sciencemag.org/cgi/content/full/science.1249061/DC1

Supplementary Materials for

Highly Crystalline Multimetallic Nanoframes with Three-Dimensional Electrocatalytic Surfaces

Chen Chen, Yijin Kang, Ziyang Huo, Zhongwei Zhu, Wenyu Huang, Huolin L. Xin, Joshua D. Snyder, Dongguo Li, Jeffrey A. Herron, Manos Mavrikakis, Miaofang Chi, Karren L. More, Yadong Li, Nenad M. Markovic, Gabor A. Somorjai, Peidong Yang,* Vojislav R. Stamenkovic*

*Corresponding author. E-mail: p_yang@berkeley.edu (P.Y.); vrstamenkovic@anl.gov (V.R.S.)

Published 27 February 2014 on *Science* Express
DOI: 10.1126/science.1249061

This PDF file includes:

Other supplementary material for this manuscript includes the following:

Movies S1 and S2

Materials and Methods

Synthesis

Synthesis of $PtNi_3$ nanopolyhedra: 20 mg $H_2PtCl_6 \cdot 6H_2O$ and 17.5 mg $Ni(NO_3)_2 \cdot 6H_2O$ were dissolved in 0.4 mL deionized water, forming a transparent solution. The solution was then added to 10 mL oleylamine in a three-necked flask at 160 °C, and the temperature was kept for 2-3 min to remove water. The reaction system was further heated up to 270 °C under Ar atmosphere. 3 min after the transparent solution turned into a black slurry, the reaction was stopped by rapidly cooling the solution down to room temperature. The yielded $PtNi_3$ nanopolyhedra were collected by centrifugation (5000 rpm).

Evolution from $PtNi_3$ nanopolyhedra to Pt_3Ni nanoframes: The $PtNi_3$ nanopolyhedra were redispersed in hexanes. The colloidal solution was kept under ambient conditions for 2 weeks, affording Pt_3Ni nanoframes. This evolution process could be accelerated following the procedures below. $PtNi_3$ nanopolyhedra (ca. 3 mg) were redipsersed in 5 mL chloroform, with 0.2 mL oleylamine added. The colloidal solution was diluted with 10 mL hexadecane, and then sonicated for 20 min, followed by heating at 120 °C for 12 hr in air. The afforded Pt_3Ni nanoframes were collected by centrifugation (8000 rpm).

Scale up preparation of Pt_3Ni nanoframes: 200 mg $H_2PtCl_6 \cdot 6H_2O$ and 175 mg $Ni(NO_3)_2 \cdot 6H_2O$ were dissolved in 4 mL deionized water, forming a transparent solution. The solution was then added to 100 mL oleylamine in a three-necked flask at 160 °C, and the temperature was kept for 2-3 min to remove water. The reaction system was further heated up to 270 °C under Ar atmosphere. 3 min after the transparent solution turned into a black slurry, the reaction was stopped by rapidly cooling the solution down to room temperature. The $PtNi_3$ nanopolyhedra collected by centrifugation (8000 rpm) were redispersed in 100 mL hexadecane (with 5 mL oleylamine, and sonicated for 20 min), then were heated at 120 °C for 12 hr in air. The Pt_3Ni nanoframes were collected by centrifugation (8000 rpm) and redispersed in chloroform. The concentration of precursor solution can be further doubled, whereas the Pt_3Ni nanoframes with larger size (~50 nm in diameter) are produced. Thus, one pot synthesis can supply material that is sufficient to prepare catalysts (20% loading) at gram-scale.

Preparation of [MTBD][NTf2] ionic-liquid: 7-methyl-1,5,7-triazabicyclo[4.4.0]dec-5-ene [MTBD] (Sigma-Aldrich) was neutralized by adding 10.6 M HNO_3 drop wise to the [MTBD]. Then, equimolar amounts of neutralized [MTBD] and lithium salt of bis(trifluoromethane)sulfonimide [NTf2] (Acros) are mixed and dissolved in DI water. The product of IL precipitated out as a viscous fluid. The IL was washed several times with DI water and then placed in a vacuum oven at 60 °C for 12 hours to remove residual water.

In-situ ambient-pressure XPS study

We found that the evolution could only proceed in air (or oxygen), but not in inert atmosphere, such as Ar (Fig. S9). We further carried out in-situ ambient-pressure XPS (AP-XPS) studies on both nanostructures to investigate the response of Pt and Ni surface concentrations to different gas environments (*30*). The variation in surface composition can further support the aforementioned compositional evolution mechanism. As

illustrated in Fig. S10A, at 120 °C, the surface composition of $PtNi_3$ polyhedra reversibly changes in response to alternating the gas environment. Specifically, the Ni fraction increases under oxygen, and the Pt percentage increases under hydrogen. Such phenomena indicate that the presence of oxygen facilitates the migration of Ni atoms to the surface. Likewise, Pt_3Ni nanoframes exhibit similar behaviors under at 120 °C (Fig. S10B), with less prominent variation amplitudes for Pt and Ni though, probably owing to the less amount of Ni in the system. It is noteworthy that the variations in surface concentrations of both samples are smaller at lower temperature (80 °C), which may be attributed to the lower migration mobility of both Pt and Ni atoms. Altogether these results confirmed that, in the presence of oxygen, the Ni atoms in $PtNi_3$ polyhedra tend to segregate to the surface, which, in combination of oxidation and dissolution of Ni species, eventually leads to the formation of Pt_3Ni phase.

Electrochemical study

Synthesized cuboctahedral Pt, PtNi nanocrystals, and Pt_3Ni nanoframes were incorporated onto carbon black (Cabot, Vulcan XC-72), and washed by ethanol. Then the organic surfactants were removed by thermal treatment in controlled atmosphere, and the nanocrystals (or nanoframes)/carbon mixture were further annealed in inert gas atmosphere at temperature below 400 °C for 12 h. Total metal loading was controlled in the range of ~20%. The actual loadings were determined by ICP-MS. The commercial 5 nm Pt/C catalyst were supplied by TKK, Tokyo, Japan and used for comparison. The catalysts were washed with 0.1 M $HClO_4$ and then were prepared to catalyst inks by adding water (from 0.5 to 1 mg catalysts/mL water), followed by a sonication of 30 min. After that, 10 to 20 μL inks were deposited glassy carbon electrode (6 mm in diameter) and dried to form a uniform thin film that was further characterized in electrochemical cell.

The $Ni(OH)_2$ modified electrodes for HER studies were prepared following the literature (*13*). The electrochemical measurements were conducted in a three-compartment electrochemical cell with a Pine rotational disk electrode (RDE) setup and an Autolab 302 potentiostat. A saturated Ag/AgCl electrode and a Pt wire were used as reference and counter electrodes, respectively. 0.1 M KOH was used as electrolyte for HER study and $HClO_4$ was used as electrolyte for rest. The sweep rates of 50 mV/s were used for CVs and HER; 20 mV/s was used for ORR measurements (RDE rotating rate of 1600 rpm). The current densities for ORR and HER were corrected by ohmic iR drop compensation during the measurements. All of the potentials are versus reversible hydrogen electrode (RHE). The stability tests (25 °C) were carried out by 10,000 cycles between 0.6 – 1.0 V from 2 to 200 mV/s. Nafion solution was used to prepare working electrodes for the stability test.

For the Pt_3Ni nanoframes/IL catalysts, a drop of IL was dropped onto the electrode covered with Pt_3Ni nanoframes catalyst layer. After 10-15 min, the electrode was dipped into 0.1M $HClO_4$, and was cycled between 0.05-0.92 V for 50 cycles under Ar, at a scan rate of 50 mV/s. After the cycling, the ORR activity was tested in fresh electrolyte. For the data shown in Fig.S22-S24, the tests were carried out on the same electrode, respectively. The stability test was carried out in the same way as described above.

O_2 solubility was measured using a Pt microelectrode made by sealing a 25 μm diameter Pt wire in a quartz capillary, as described in literature(*6*).

Theoretical study

Spin-polarized, self-consistent density functional theory calculations are performed using DACAPO(*31, 32*). A 2 x 2 unit cell is used to construct a six layer $Pt_3Ni(111)$ slab (24 slab atoms). This corresponds to a surface coverage of 1/4 ML when there is only one adsorbate per unit cell. The unit cell is repeated in a super cell geometry with successive slabs separated by a vacuum region of at least 10 Å. The optimized bulk lattice constant for Pt_3Ni is calculated to be 3.89 Å, which compares well with an experimental value of 3.84 Å. Adsorption is allowed on only one of the two exposed surfaces, with the electrostatic potential adjusted accordingly. The top four layers of the slab are relaxed. The surface Brillouin zone is sampled at 18 special Chadi-Cohen k-points(*33*). The Kohn–Sham one-electron valence states are expanded in a basis of plane waves with kinetic energies up to 25 Ry, and ionic cores are described by ultrasoft Vanderbilt pseudopotentials(*34*). The exchange-correlation potential and energy are described self-consistently using the GGA-PW91 functional(*35, 36*). The electron density is determined by iterative diagonalization of the Kohn–Sham Hamiltonian, Fermi-population of the Kohn–Sham states (k_BT = 0.1 eV), and Pulay mixing of the resulting electronic density. Total energies are then extrapolated to k_BT = 0 eV.

The binding energies of O are calculated on the Pt_3Ni slab after replacing the top one, two, or three layers of the slab with pure Pt and subjecting the surfaces to lateral compressive strain (0, 1, 2, or 3% with respect to bulk Pt_3Ni). The different slab models are chosen to simulate varying degrees of Pt segregation to the surface. We also calculate the binding energy of O on a Pt(111) surface which was artificially set to have the same lattice constant as bulk Pt_3Ni, and then compressed as the other surfaces (at 0% strain, the lattice constant is 3.89 Å). This is used to model the extreme case where the number of Pt layers is enough there is no ligand effect modifying the surface properties. The differential binding energies of O are calculated at 0.25 ML coverage with respect to the clean, compressed, relaxed surfaces ($E_{substrate}$) and the respective free adsorbate in the gas phase ($E_{gas\text{-}phase\ adsorbate}$), i.e., $E_b = E_{total} - E_{substrate} - E_{gas\text{-}phase\ adsorbate}$, where E_{total} is the total energy of the slab with the adsorbate(s) adsorbed on them.

To understand the enhanced activity of the Pt_3Ni nanoframes, we performed periodic, self-consistent density functional theory calculations (DFT-GGA) to evaluate the binding energy of O on the frame surfaces. We modeled the frames as $Pt_3Ni(111)$ surfaces with 1, 2, or 3 Pt overlayers. Similarly, we model the Pt/C catalysts as Pt(111) surfaces. The surface of small nanoparticles contracts with respect to the bulk lattice constant. Therefore, to understand how this contraction might affect the adsorption of O, we studied adsorption under 1, 2, or 3% lateral compressive strain in the surfaces. In a previous study(*37*), using a very similar calculation setup and methodology to this work, a theoretical volcano curve for oxygen reduction was generated using the binding energy of O as a reactivity descriptor, and finding that the optimal O binding energy is -3.57 eV (at ¼ ML coverage). This optimal value corresponds to the point in which O_2 dissociation kinetics are balanced with O hydrogenation kinetics. The oxygen reduction activity of surfaces which bind O stronger than this optimal value is limited by difficulty in hydrogenating O, while activity of surfaces which bind O weaker than this optimal is limited by O_2 dissociation. Pt(111) has a calculated O binding energy of -3.81 eV, significantly stronger than the optimal value.

Our results for the binding energy of O at 0.25 ML coverage on the Pt-terminated $Pt_3Ni(111)$ surfaces are shown as a function of lateral compressive strain in Fig. S15. The results demonstrate that the Pt-terminated surfaces bind oxygen near the optimal binding energy, and importantly, significantly weaker than Pt(111). If the $Pt_3Ni(111)$ possesses as single Pt overlayer, it binds closest to the optimal value with 0% compressive strain. With compressive strain, the binding of O weakens monotonically and diverges from the optimal. However, with two or three Pt overlayers, the uncompressed surface binds O slightly stronger than the optimal, and it is most close to the optimal value with a slight 1% compressive strain. With additional compression, these two surfaces do not diverge from the optimal binding energy by much. With the further increasing thickness of Pt overlayers, there would be no ligand effect modifying the surface property, leading to weaker binding of O and ultimately leading to reduced activity, which is consistent to the experimental observations(*9*). Overall, these results show that the Pt-terminated $Pt_3Ni(111)$ surfaces with two or three Pt overlayers should be more active than pure Pt(111) regardless of any compression because the binding of O is weakened sufficiently so that O hydrogenation is facile, while not too weak for O_2 dissociation to be hindered. With only a single Pt overlayer, though, the surface should be more active than Pt(111) at 0% compression. With higher compression, the binding energy of O weakens such that O_2 dissociation kinetics will, likely, hinder oxygen reduction activity.

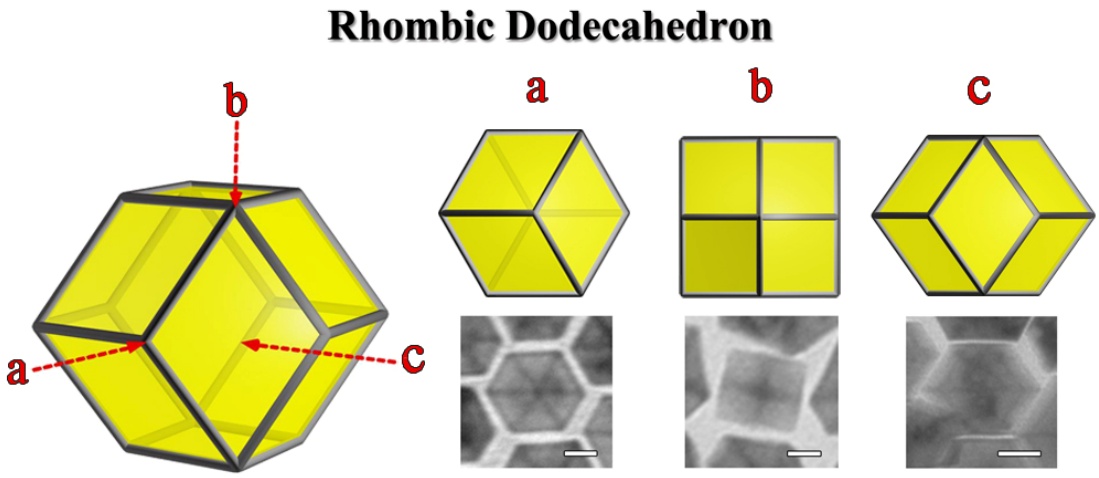

Fig. S1. Schematic illustrations and corresponding TEM images of a rhombic dodecahedron (scale bar: 5 nm).

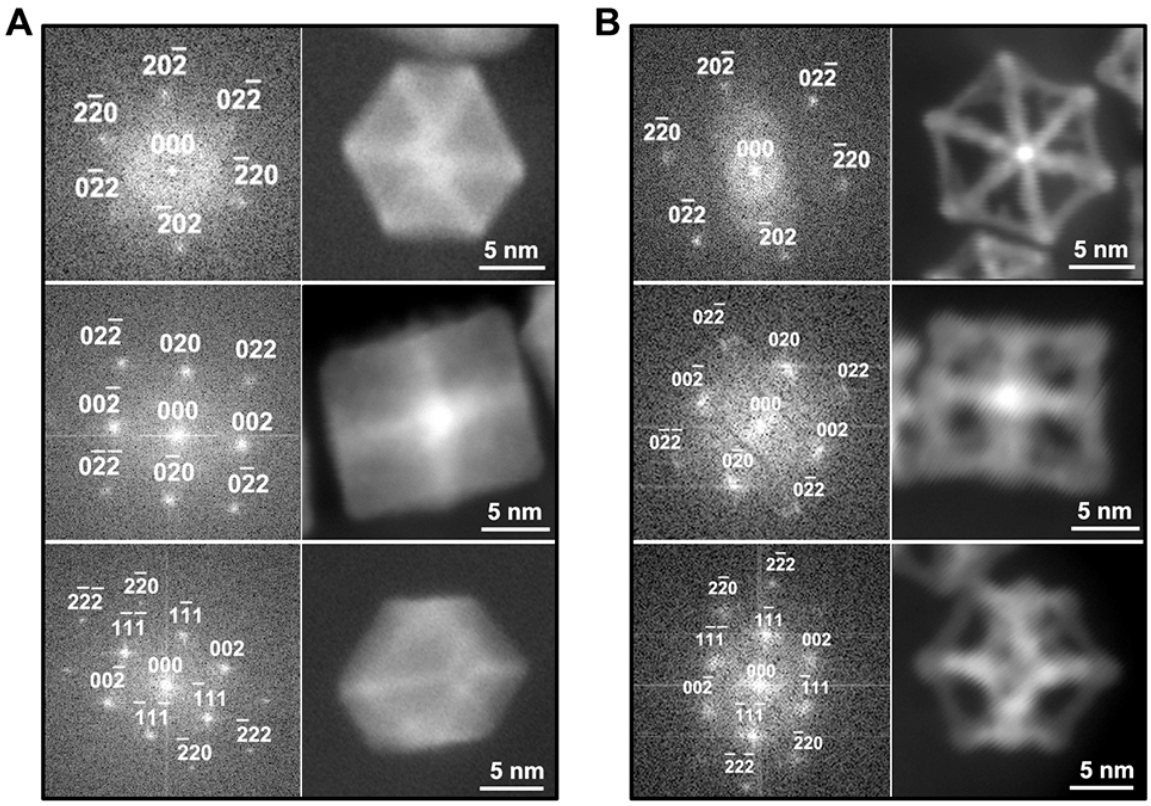

Fig. S2. Fast Fourier transform (FFT) patterns and STEM images of (A) solid PtNi3 polyhedra and (B) hollow Pt3Ni nanoframes, corresponding to the HRTEM images in Fig. 2A and B.

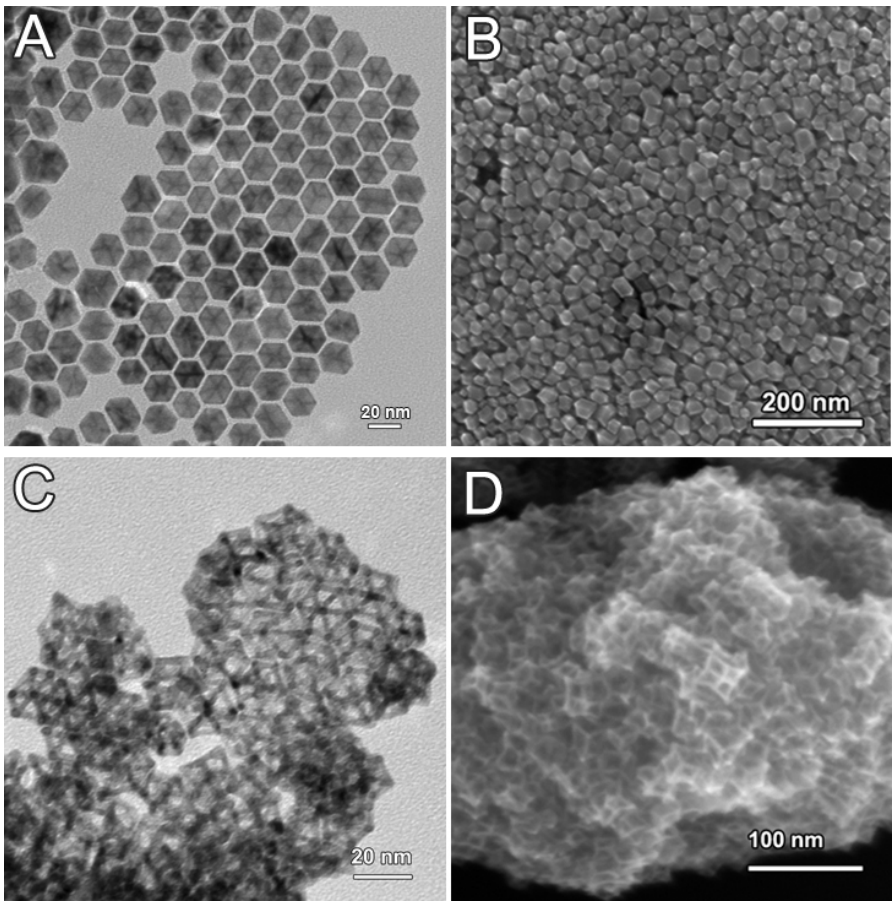

Fig. S3. (A) TEM and (B) SEM images of parent $PtNi_3$ polyhedra. (C) TEM and (D) SEM images of Pt_3Ni nanoframes yielded after 2 weeks under ambient conditions.

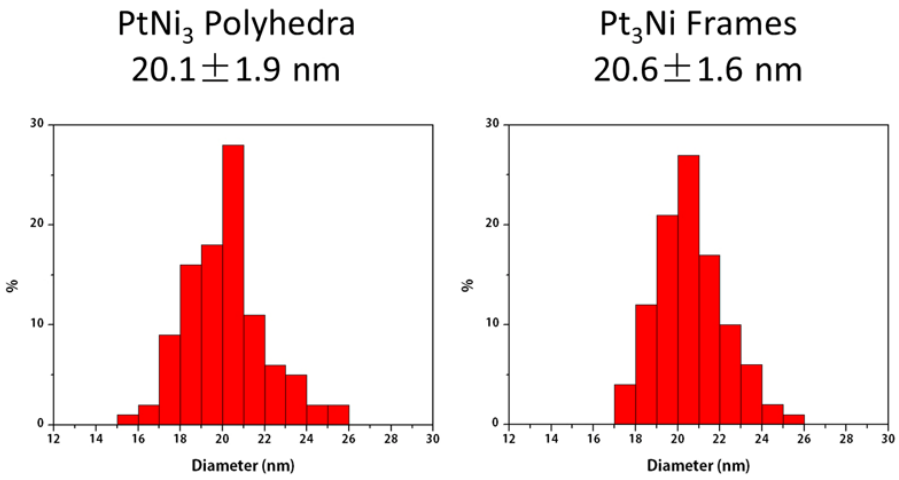

Fig. S4. Size distribution of the precursor $PtNi_3$ polyhedra and the product Pt_3Ni frames.

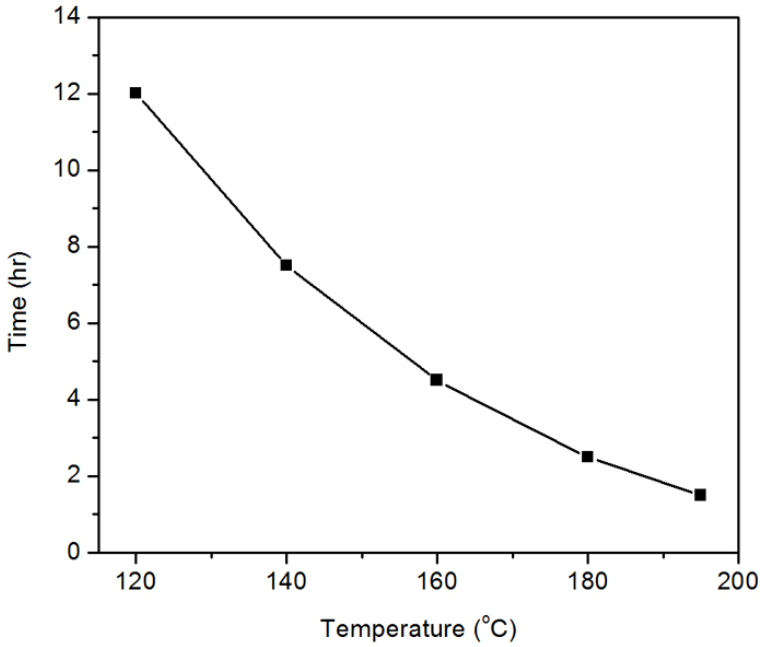

Fig. S5. Plot of evolution time (from $PtNi_3$ polyhedra to Pt_3Ni hollow frames) against temperature.

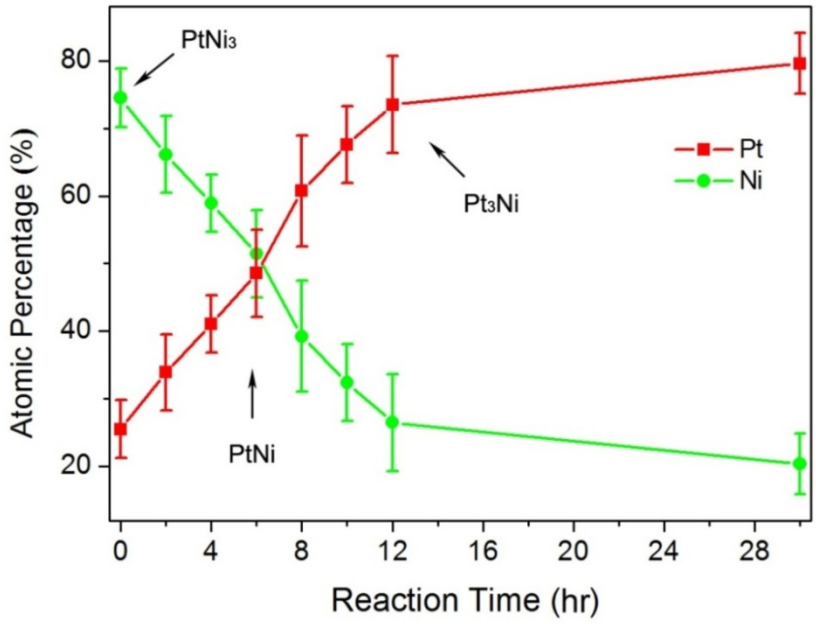

Fig. S6. Correlation between molar ratios of Pt/Ni and reaction time at 120°C, during the evolution process.

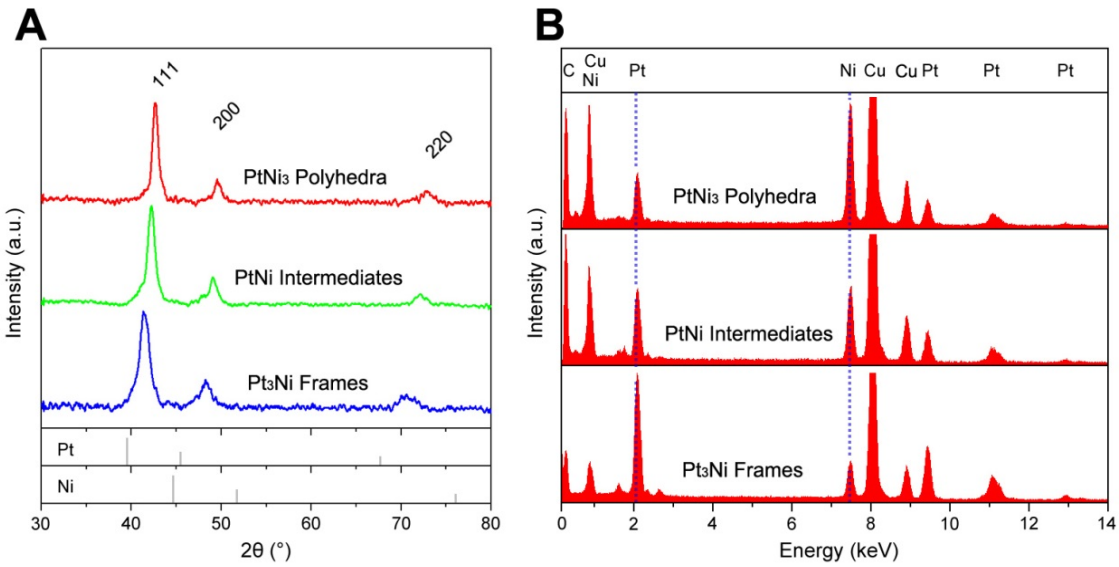

Fig. S7. Compositional characterizations of the samples ($PtNi_3$ polyhedra, PtNi intermediates and Pt_3Ni nanoframes) obtained at three representative stages during the evolution process: (A) XRD patterns suggesting the sample changing from Ni-rich alloys to Pt-rich; (B) EDX spectra revealing the composition evolving from $PtNi_3$ to PtNi, and further to Pt_3Ni (the peaks for C and Cu come from the TEM grid).

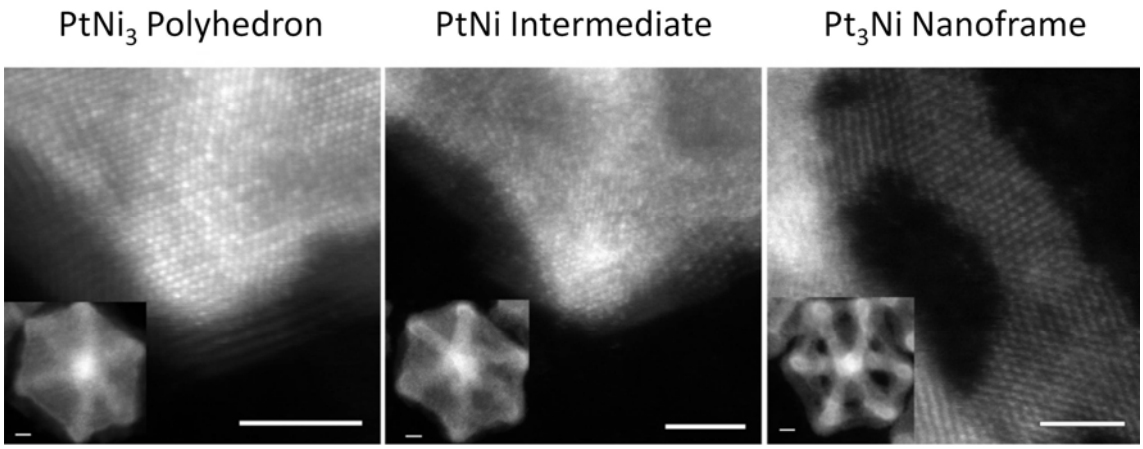

Fig. S8. Atomic-resolution HAADF-STEM images of the samples of three representative stages, showing that the Pt ratio is higher on the edge than that in the interior (for the initial $PtNi_3$ precursor and PtNi intermediates), while the Pt_3Ni product exhibits a homogeneous distribution of both Pt and Ni. (Scale bar: 2 nm)

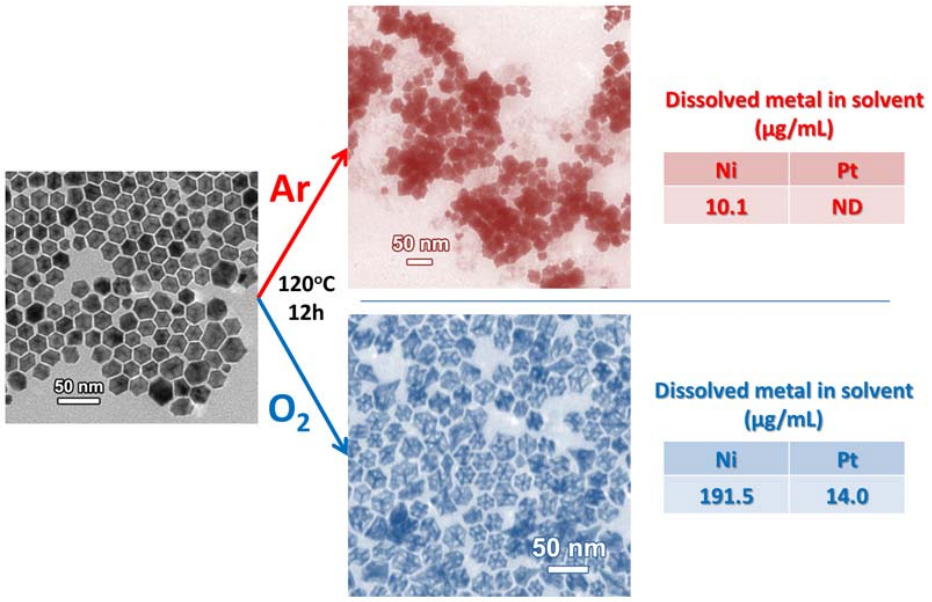

Fig. S9. Reactions carried out in different atmospheres. It can be seen that $PtNi_3$ polyhedra heated in the presence of oxygen transform into Pt_3Ni nanoframes, while those in argon atomsphere remain basically unchanged in morphology, though with some aggregate formation. The tables on the right summarize the concentrations of dissolved Pt and Ni (detected by ICP-MS) in the solvent. The sample treated in oxygen exhibits significant dissolution of both Pt and Ni; in comparison, the one treated in argon only shows minor dissolution of Ni.

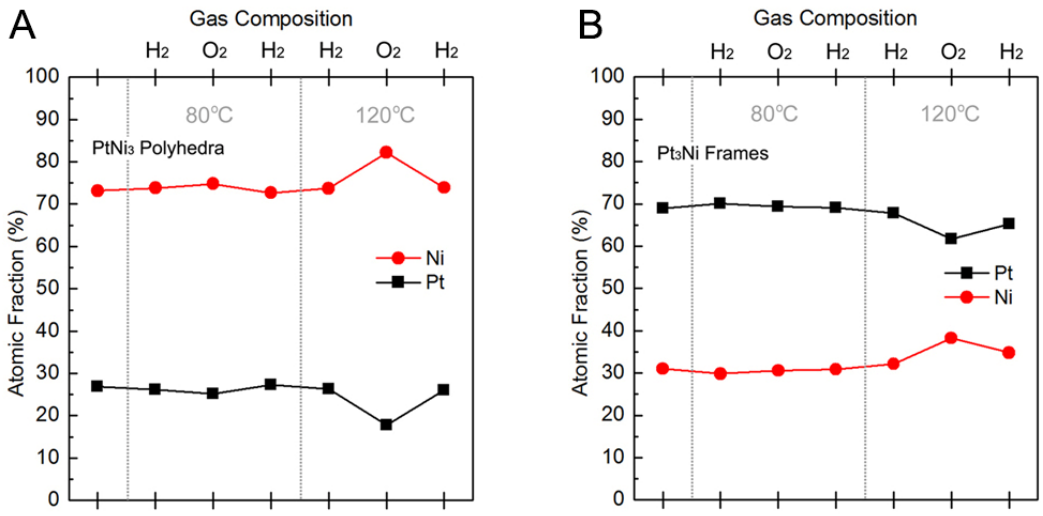

Fig. S10. Variations in the surface Pt and Ni concentrations of (A) $PtNi_3$ polyhedra and (B) Pt_3Ni nanoframes in response to changes in the gas environment obtained by AP-XPS. Pt and Ni concentrations are calculated by integrating the peak areas in Pt 4f and Ni 3p spectra after fitting the peaks and correction with the cross-section values. The spectra were acquired with incident X-ray energy of 490 eV that generates photoelectrons with ~420 eV kinetic energy, corresponding to ~0.9 nm probing depth.

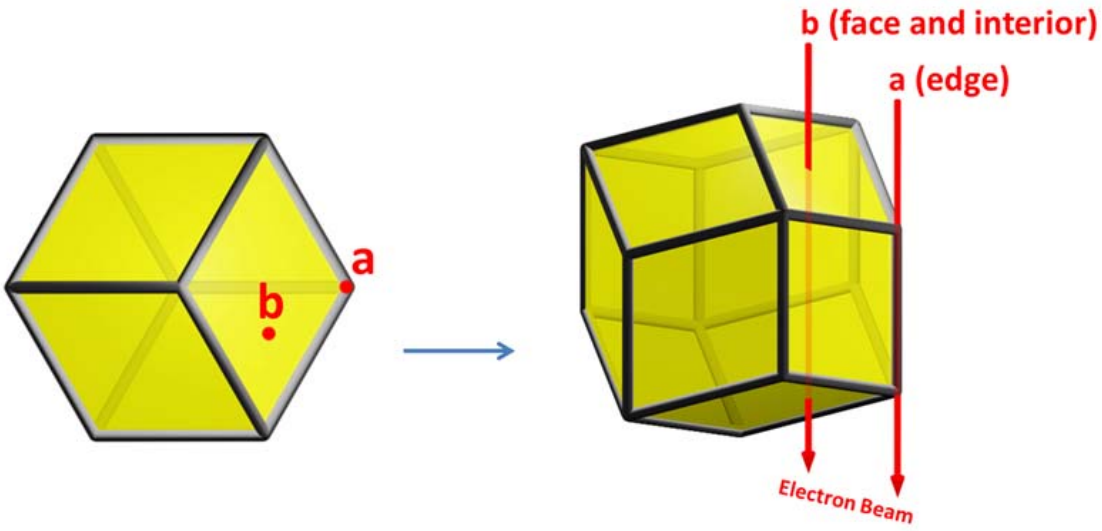

Pt Atomic %	$PtNi_3$ Polyhedra	PtNi Intermediates	Pt_3Ni Frames
(a) Edge	28.3±4.9 %	51.2±8.1 %	73.5±7.2 %
(b) Face and Interior	13.4±4.8 %	26.3±7.0 %	-

Fig. S11. Site-specific EDX analysis results for the samples of three representative stages, showing that the Pt ratio is higher on the edge than that in the interior. The EDX beam size for both site a and b is 1 nm, which is comparable to the size of the particle edges (2 nm).

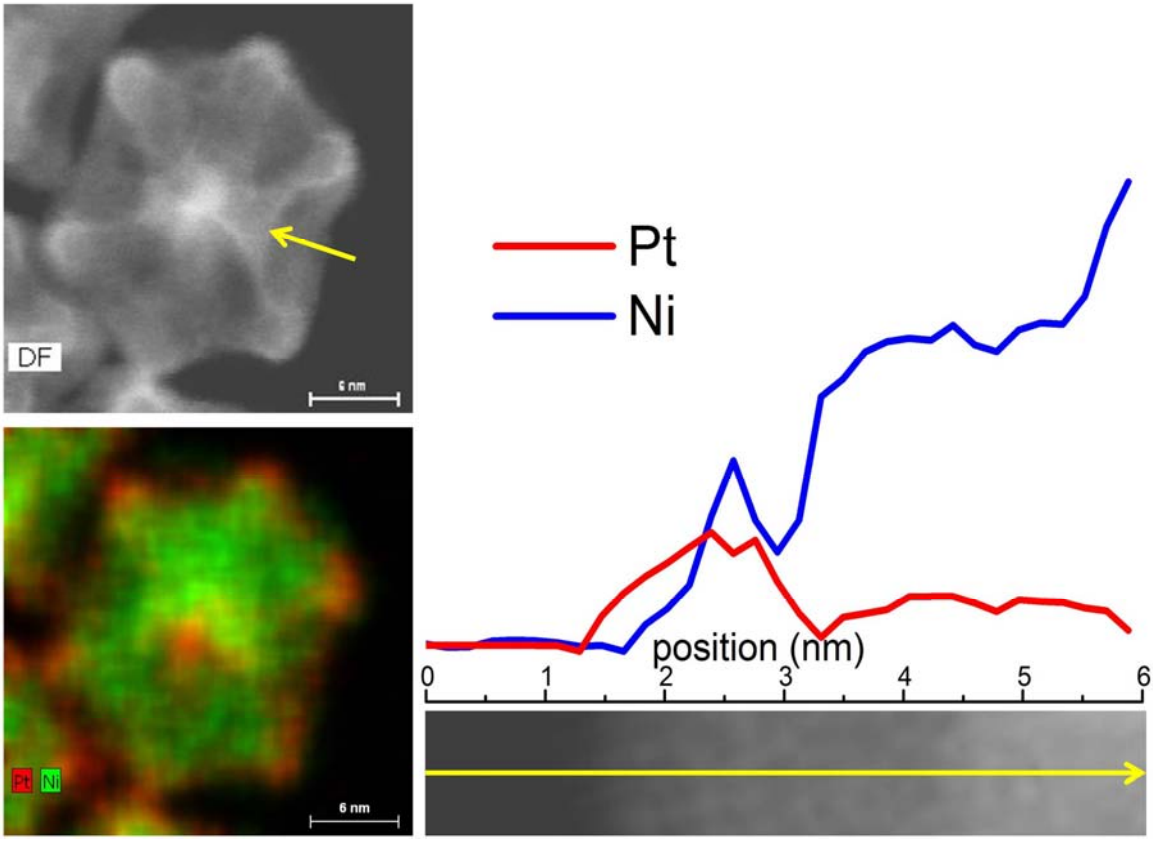

Fig. S12. HAADF-STEM image and corresponding EDX data (mapping and line-scan) of solid $PtNi_3$ polyhedron. The strong atomic number (*Z*) contrast in HAADF-STEM image indicates that average atomic number of elements on the edges is higher than that in the core of $PtNi_3$ polyhedron. The EDX map clearly confirms the observation from STEM image: the edges have much higher Pt content than the core. The EDX line-profile shows that on the edges the Pt:Ni ratio is approximately 1:1 whereas Pt is slightly rich on surface, and in the core the Ni content is significantly higher than Pt, which is in good agreement with STEM image and EDX map.

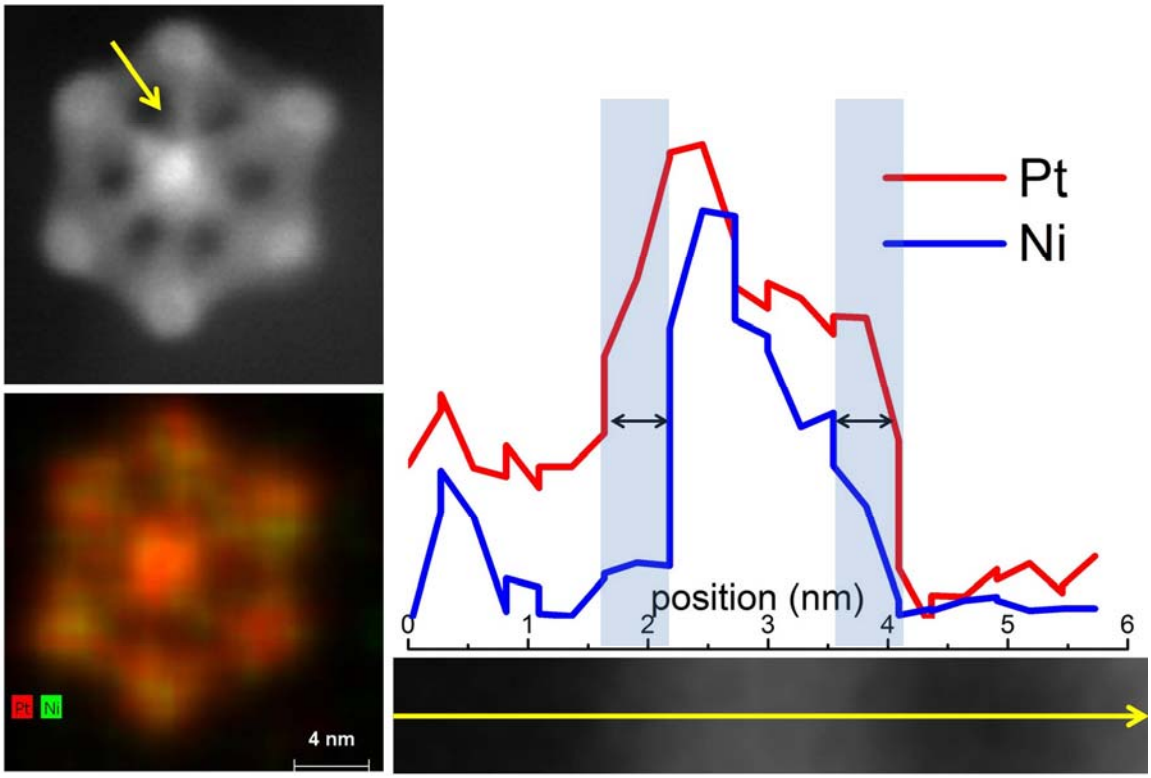

Fig. S13. HAADF-STEM image and corresponding EDX data (mapping and line-scan) of annealed hollow Pt_3Ni nanoframe. The EDX map shows that Pt is the dominant content in the nanoframe. The line-profile indicates that the Pt-Skin on the edges of the frames is approximately 0.5 nm thick, corresponding to at least 2 monolayers of Pt. The dark regions in STEM image corresponding to those of the EDX map have no elemental (Pt and Ni) signal. Moreover, the EDX line-scan intensities in the interior (dark regions) confirm the presence of the hollow interior.

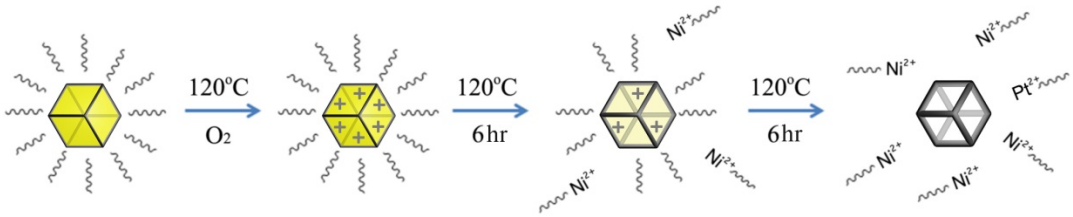

Fig. S14. Schematic illustration for the chemical and structural evolution process.

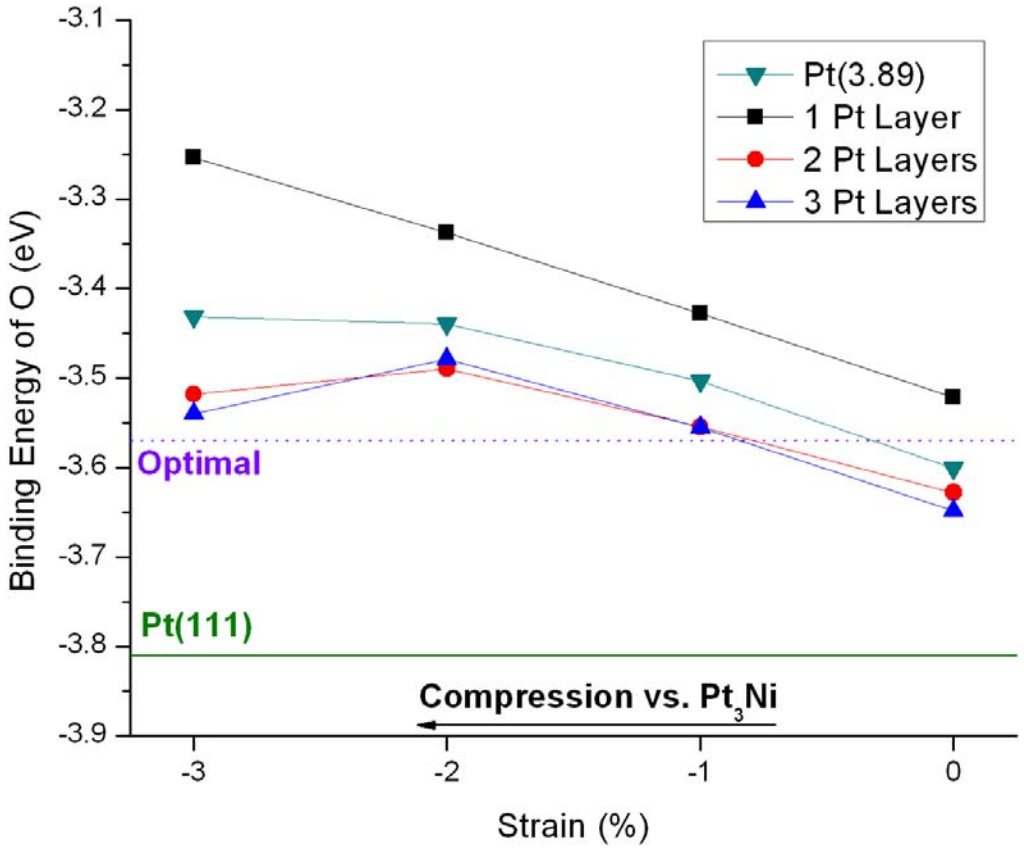

Fig. S15. Binding energy of O on Pt-terminated $Pt_3Ni(111)$ surfaces as a function of compressive strain (with respect to bulk Pt_3Ni) and number of Pt overlayers. In teal, the binding energy of O on Pt(111) which is compressed to the lattice constant of Pt_3Ni (3.89 Å is denoted as 0% strain). The purple, dashed, horizontal line shows the theoretically-determined optimal binding energy of O from the previous work (*37*). The green solid line shows the binding energy of O on uncompressed Pt(111).

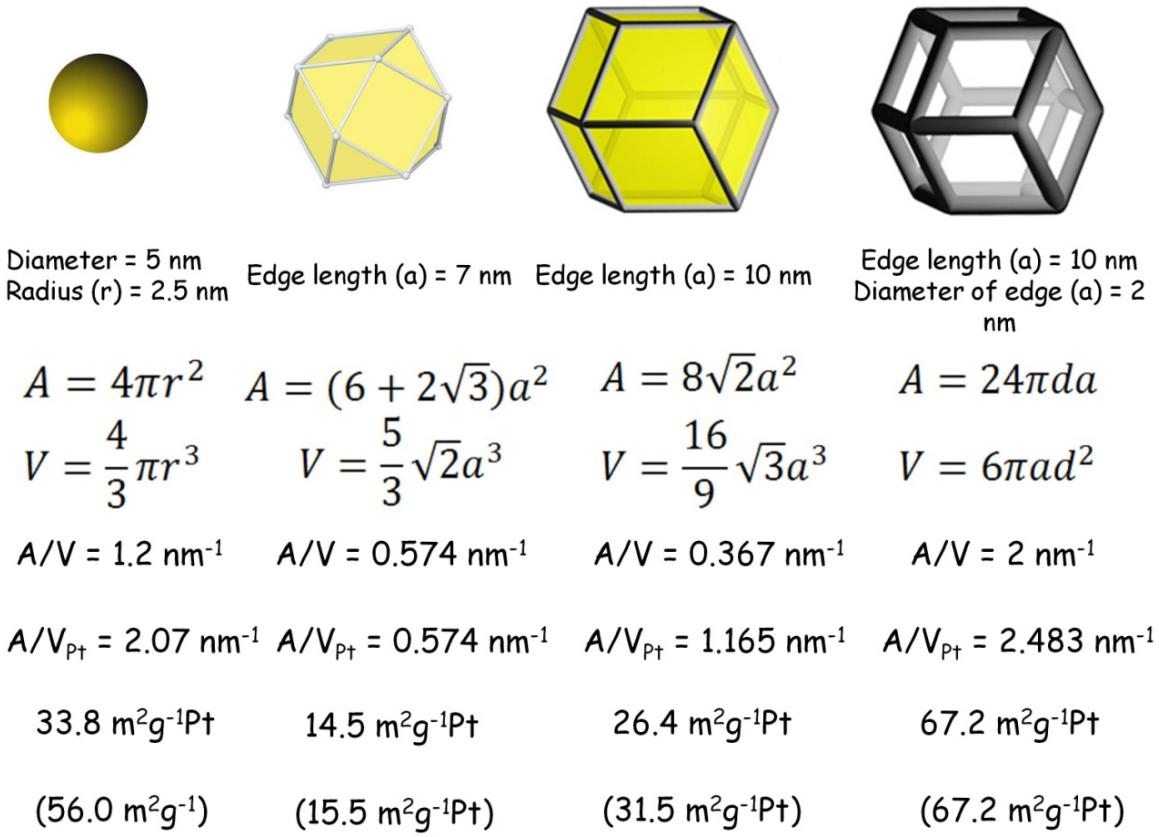

Fig. S16. Calculation of surface area (A), volume (V), and surface area to volume ratio (A/V) of sphere, cuboctahedron, solid rhombic dodecahedron, and hollow frame transformed from a solid rhombic dodecahedron. In the 2 bottom rows, the corresponding surface areas of PtNi near spherical nanocrystals with a diameter of 5 nm, Pt cuboctahedra with an edge length of 7 nm, $PtNi_3$ solid rhombic dodecahedra with an edge length of 10 nm, and Pt_3Ni nanoframes with an edge length of 10 nm, are obtained experimentally by electrochemical evaluation (i.e. CO-stripping). In the brackets, the surface areas are derived from the surface area experimentally obtained on Pt_3Ni nanoframes and the respective A/V_{Pt} ratio of each morphology. The experimental measured surface areas are in good agreement with the calculations. The near-spherical PtNi and cuboctahedral Pt nanocrystals are prepared following the literature (*9, 15*).

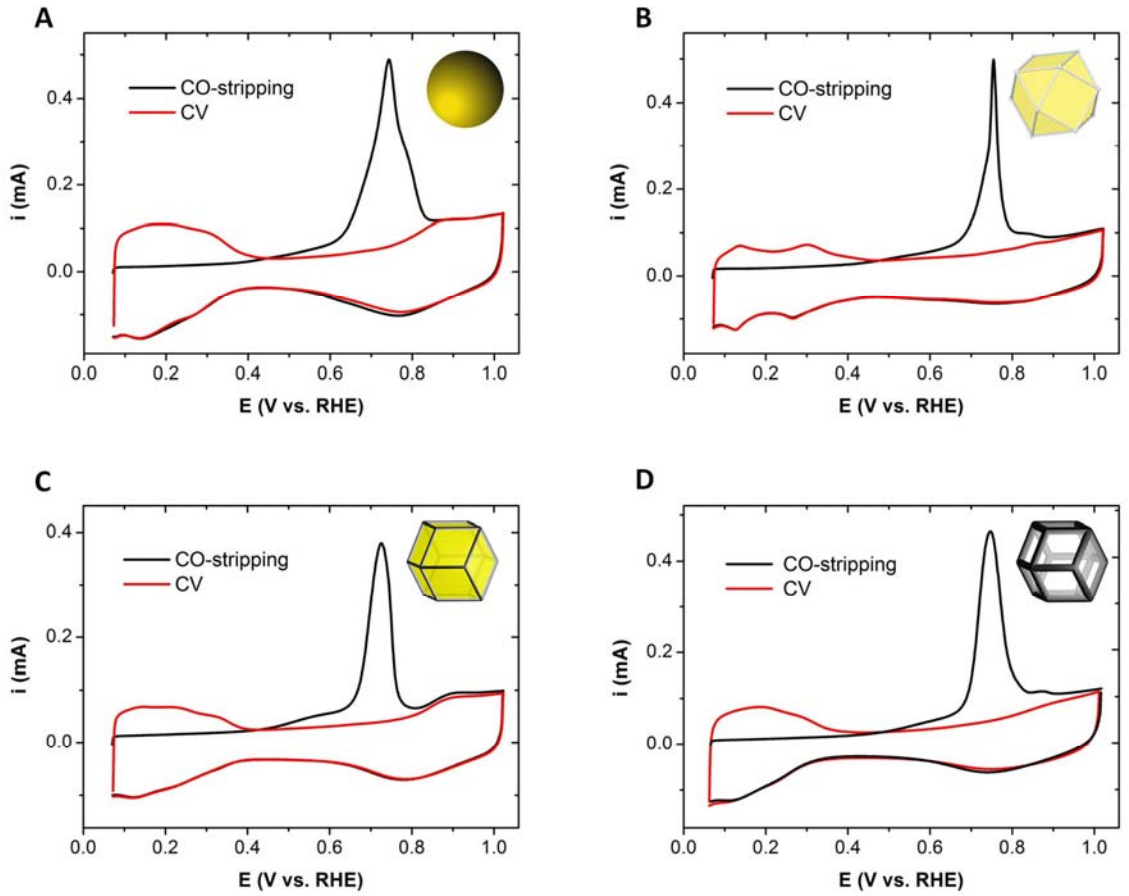

Fig. S17. CV curves and CO-stripping curves of (A) near spherical PtNi nanocrystals, (B) Pt cuboctahedra, (C) solid $PtNi_3$ rhombic dodecahedra, and (D) hollow Pt_3Ni nanoframes.

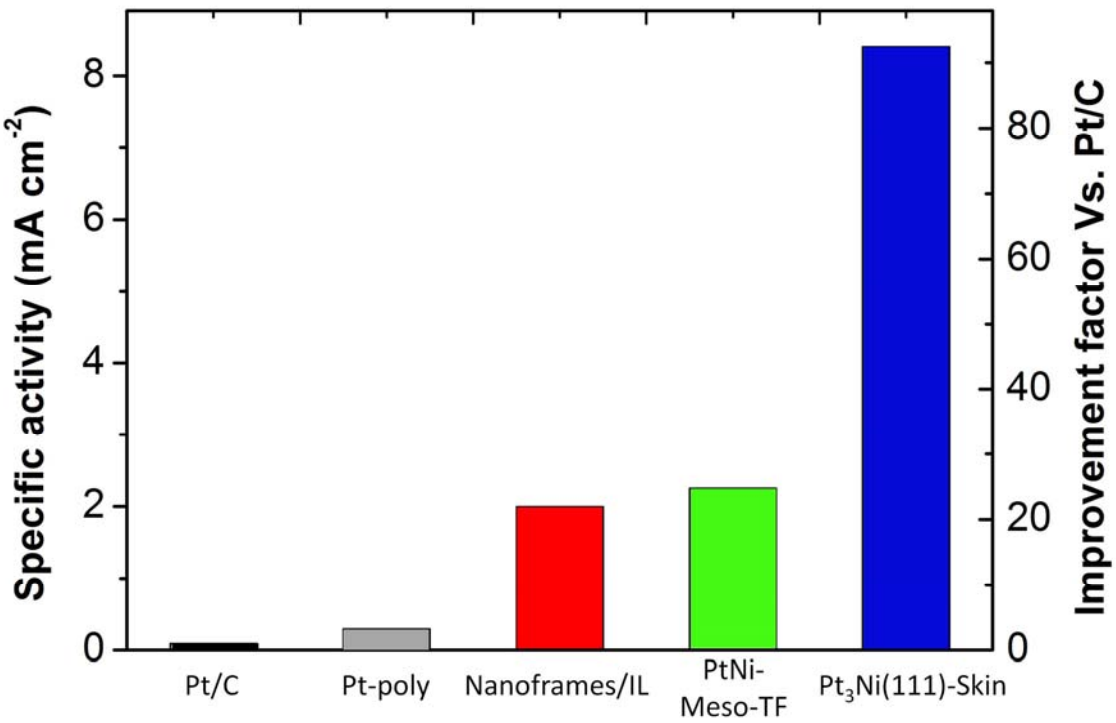

Fig. S18. Bar chart showing the specific activities [normalized by ECSA(CO_{ad})] of Pt/C, Pt poly-crystal electrode (*3*), IL-encapsulated Pt_3Ni nanoframes/C, PtNi-Meso-TF (*3*), and $Pt_3Ni(111)$-Skin electrode (*3*), and corresponding improvement factors vs. Pt/C. The activities were measured at 0.95 V (vs. RHE), in 0.1 M $HClO_4$, on an RDE (1600 rpm).

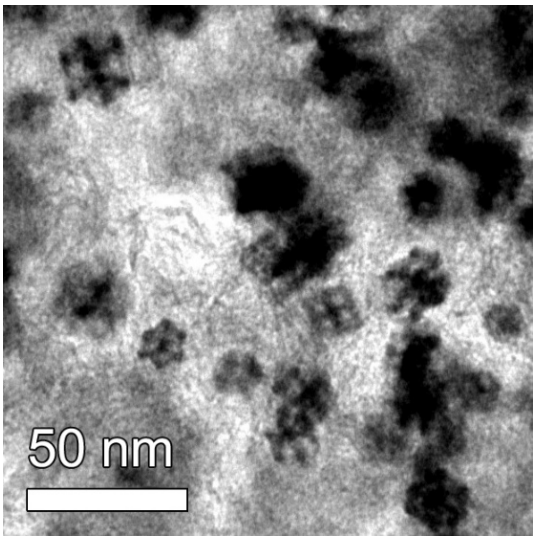

Fig. S19. TEM image of Pt_3Ni nanoframes/C catalysts annealed at 400°C in Ar.

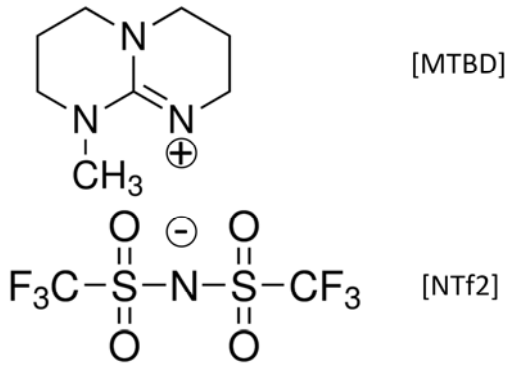

Fig. S20. The structure of [MTBD][NTf2] ionic liquid.

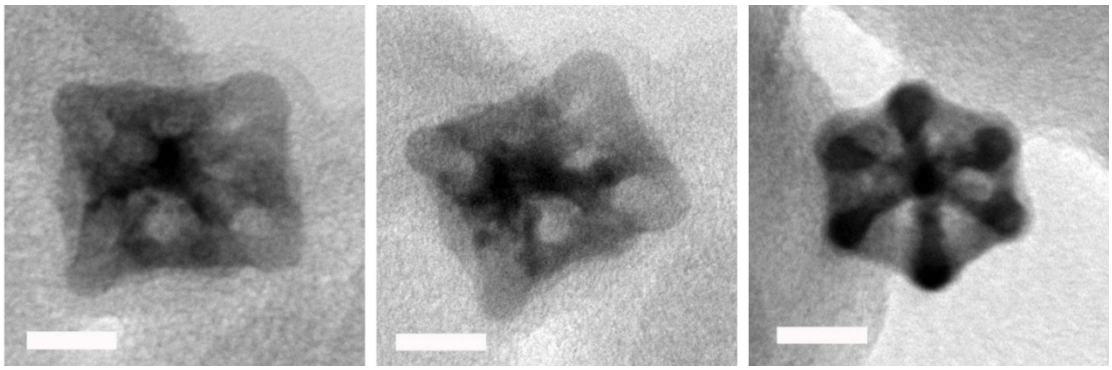

Fig. S21. TEM images of ionic liquid-encapsulated Pt_3Ni nanoframes. (Scale bar: 5 nm). Ionic liquid is visible as a light gray coating that surrounds nanoframe.

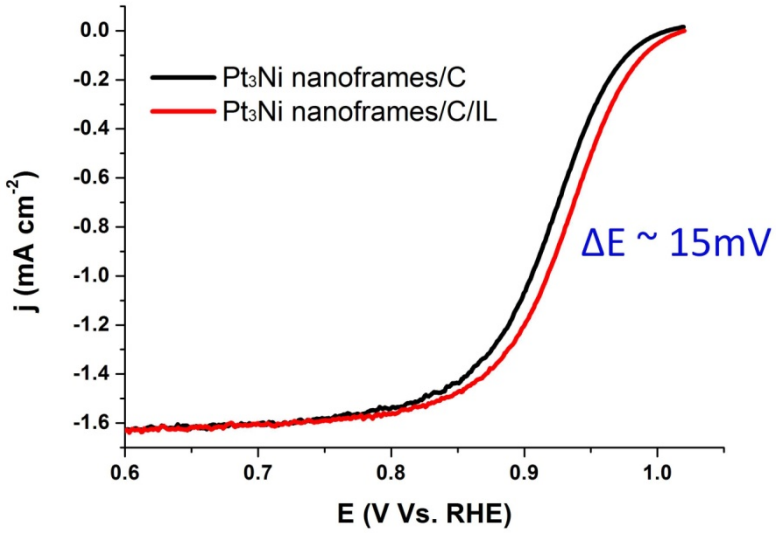

Fig. S22. ORR polarization curves on Pt_3Ni nanoframes/C catalysts, with and without ionic liquid (IL).

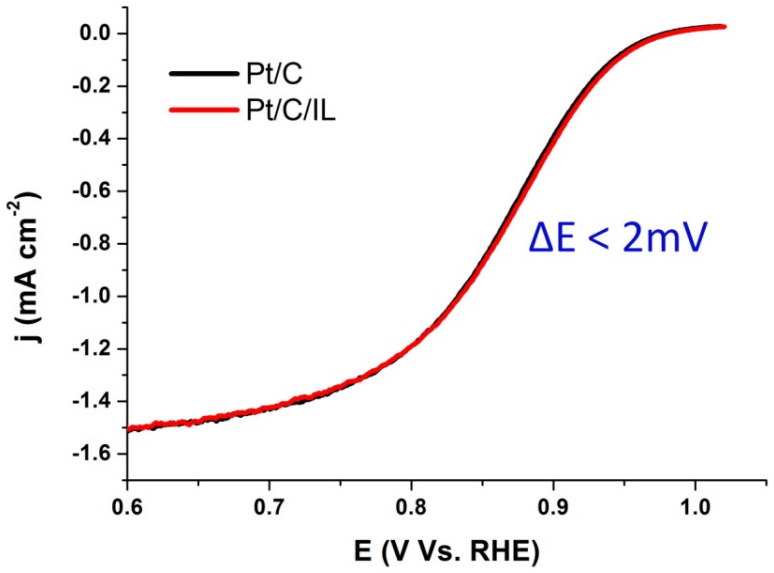

Fig. S23. ORR polarization curves on Pt/C catalysts, with and without IL, showing that after washing with electrolyte the Pt/C catalysts cannot retain IL to have a sustained enhancement.

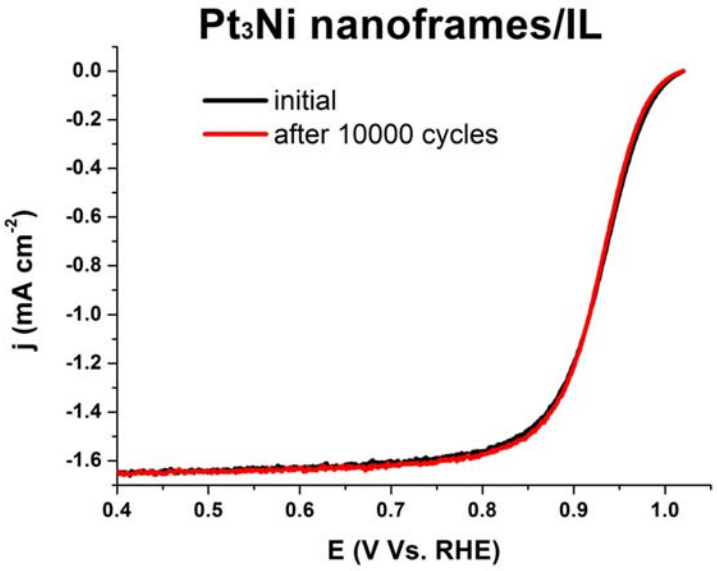

Fig. S24. ORR polarization curves on Pt_3Ni nanoframes/C catalysts with IL, showing that the catalysts are stable after 10,000 cycles.

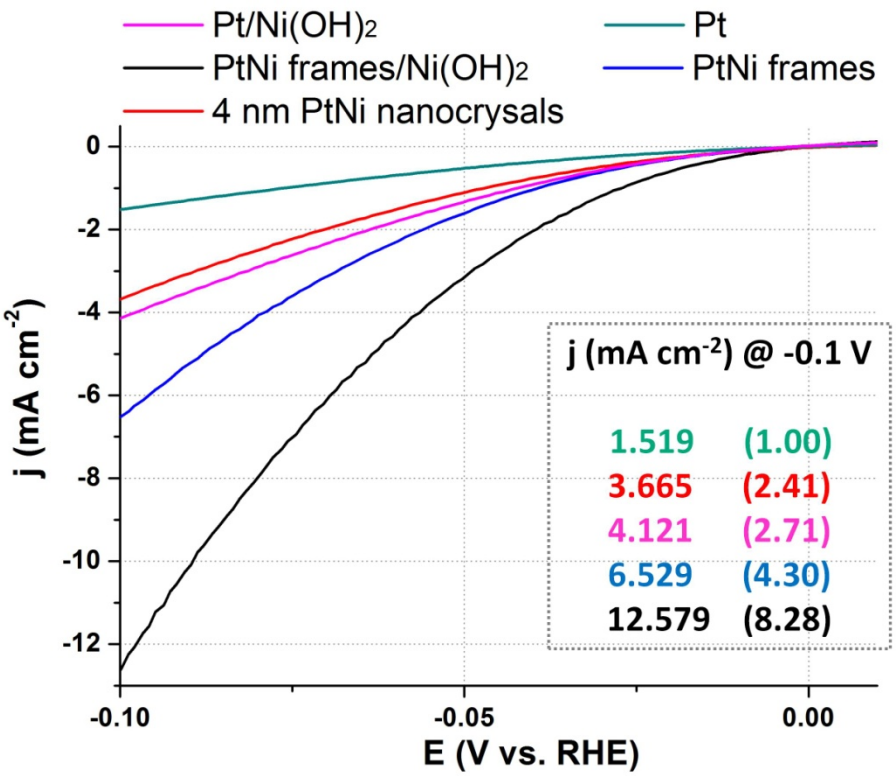

Fig. S25. Hydrogen evolution reaction polarization curves on Pt/C, 4 nm near-spherical PtNi/C, and Pt_3Ni nanoframes/C catalysts, as well as $Ni(OH)_2$ modified Pt/C and Pt_3Ni nanoframes/C catalysts. The activities in terms of current density at -0.1 V are summarized. The numbers in brackets are corresponding improvement factors vs. Pt/C.

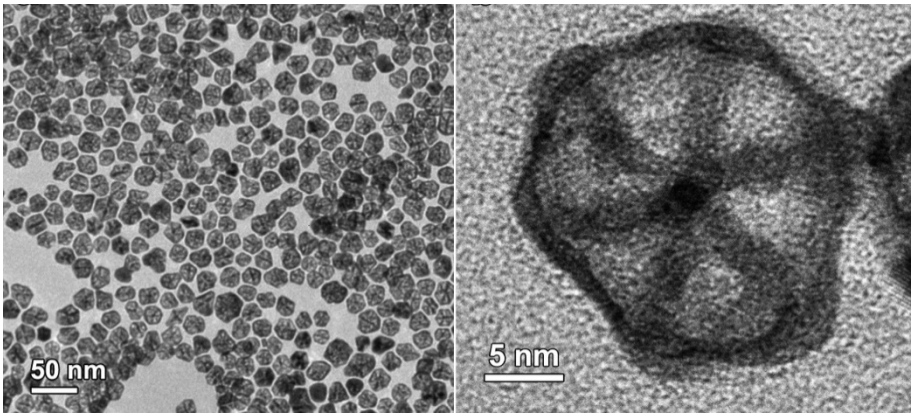

Fig. S26. Transmission electron microscopy images of hollow frame nanostructures formed in Pt-Co bimetallic system.

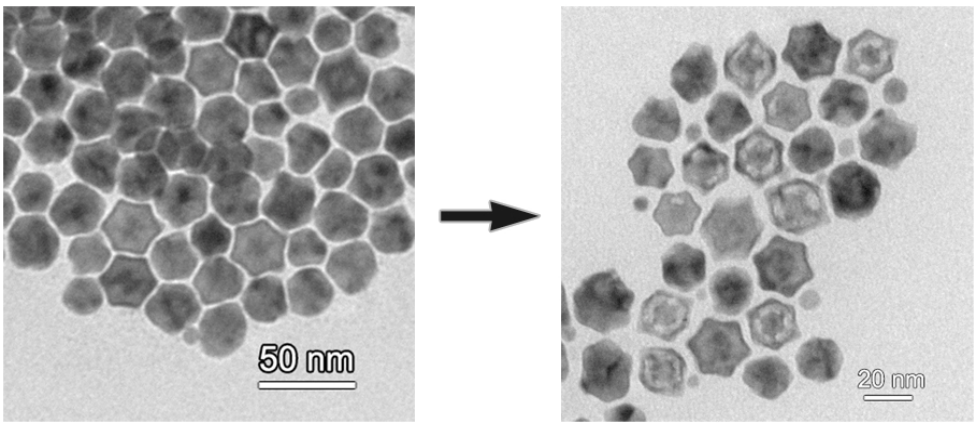

Fig. S27. Structural evolution observed in Pt-Cu bimetallic systems.

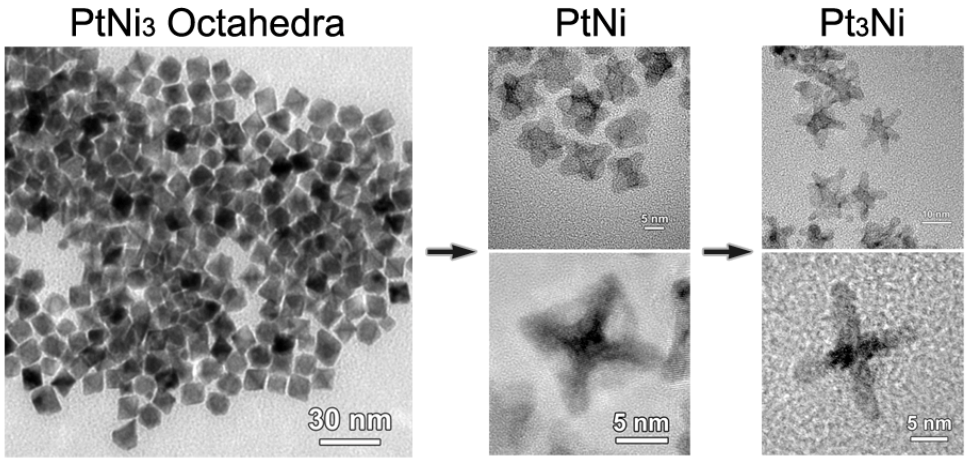

Fig. S28. $PtNi_3$ octahedra transforming into PtNi concave octahedra, and finally into Pt_3Ni hexapods, similar to previous report (*12*).

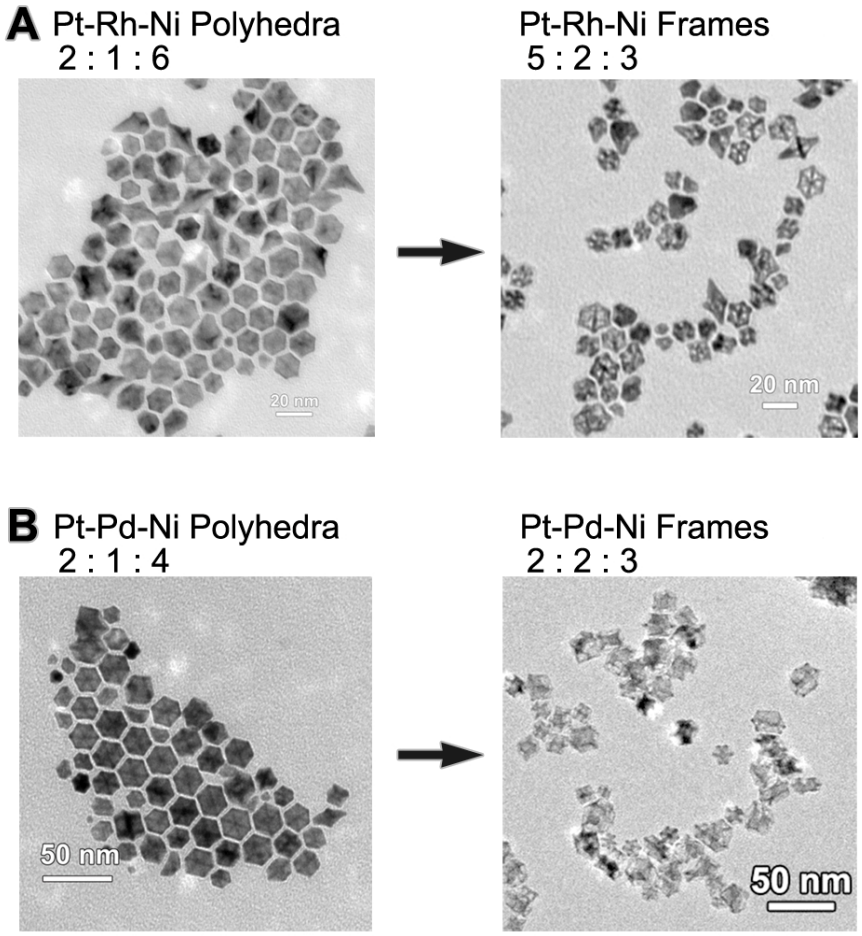

Fig. S29. Structural evolution observed in ternary metallic systems. (A) Pt-Rh-Ni and (B) Pt-Pd-Ni alloys evolving from solid rhombic dodecahedra into frames, with the size and geometry preserved while chemical composition altered.

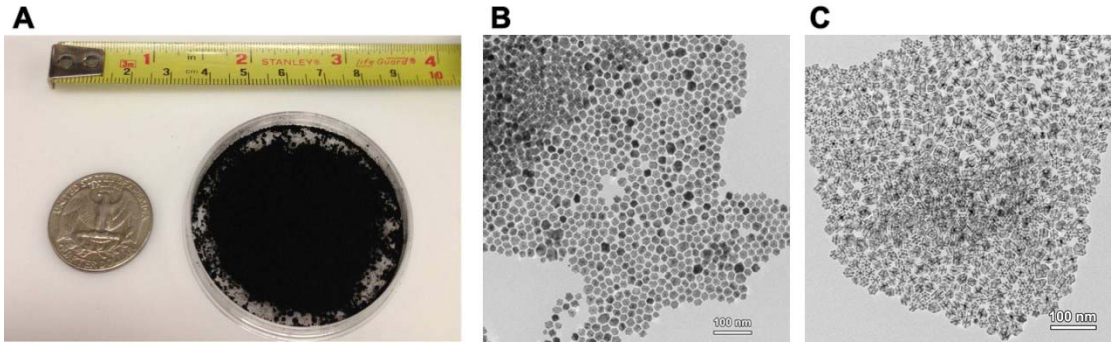

Fig. S30. (A) Picture of ~1 g Pt_3Ni nanoframes catalysts (20% Pt-loading on carbon XC-72), TEM images of (B) $PtNi_3$ solid rhombic dodecahedra and (C) Pt_3Ni nanoframes obtained from a scaled-up synthesis.

Table S1: Ratios between electrochemical surface area (ECSA) from integrated charge obtained by electrooxidation of adsorbed CO_{ad} and underpotentially deposited hydrogen (H_{upd}).

	Pt/C	5nm solid PtNi	Pt_3Ni nanoframes
$ECSA(CO_{ad})/ECSA(H_{upd})$	1.00	1.25	1.52

Movie S1

Rotation of a Pt_3Ni nanoframe - 1

Movie S2

Rotation of a Pt_3Ni nanoframe - 2

References

1. V. R. Stamenkovic, B. Fowler, B. S. Mun, G. Wang, P. N. Ross, C. A. Lucas, N. M. Marković, Improved oxygen reduction activity on $Pt_3Ni(111)$ via increased surface site availability. *Science* **315**, 493–497 (2007). doi:10.1126/science.1135941 Medline

2. S. Guo, S. Zhang, S. Sun, Tuning nanoparticle catalysis for the oxygen reduction reaction. *Angew. Chem. Int. Ed.* **52**, 8526–8544 (2013). doi:10.1002/anie.201207186 Medline

3. D. F. van der Vliet, C. Wang, D. Tripkovic, D. Strmcnik, X. F. Zhang, M. K. Debe, R. T. Atanasoski, N. M. Markovic, V. R. Stamenkovic, Mesostructured thin films as electrocatalysts with tunable composition and surface morphology. *Nat. Mater.* **11**, 1051–1058 (2012). Medline

4. D. F. van der Vliet, C. Wang, D. Li, A. P. Paulikas, J. Greeley, R. B. Rankin, D. Strmcnik, D. Tripkovic, N. M. Markovic, V. R. Stamenkovic, Unique electrochemical adsorption properties of Pt-skin surfaces. *Angew. Chem. Int. Ed.* **51**, 3139–3142 (2012). doi:10.1002/anie.201107668 Medline

5. J. Snyder, K. Livi, J. Erlebacher, Oxygen reduction reaction performance of [MTBD][beti]-encapsulated nanoporous NiPt alloy nanoparticles. *Adv. Funct. Mater.* **23**, 5494–5501 (2013). doi:10.1002/adfm.201301144

6. J. Snyder, T. Fujita, M. W. Chen, J. Erlebacher, Oxygen reduction in nanoporous metal-ionic liquid composite electrocatalysts. *Nat. Mater.* **9**, 904–907 (2010). doi:10.1038/nmat2878 Medline

7. J. Erlebacher, M. J. Aziz, A. Karma, N. Dimitrov, K. Sieradzki, Evolution of nanoporosity in dealloying. *Nature* **410**, 450–453 (2001). doi:10.1038/35068529 Medline

8. P. J. Ferreira, G. J. la O', Y. Shao-Horn, D. Morgan, R. Makharia, S. Kocha, H. A. Gasteiger, Instability of Pt/C electrocatalysts in proton exchange membrane fuel cells - A mechanistic investigation. *J. Electrochem. Soc.* **152**, A2256–A2271 (2005). doi:10.1149/1.2050347

9. C. Wang, M. Chi, D. Li, D. Strmcnik, D. van der Vliet, G. Wang, V. Komanicky, K. C. Chang, A. P. Paulikas, D. Tripkovic, J. Pearson, K. L. More, N. M. Markovic, V. R.

Stamenkovic, Design and synthesis of bimetallic electrocatalyst with multilayered Pt-skin surfaces. *J. Am. Chem. Soc.* **133**, 14396–14403 (2011). doi:10.1021/ja2047655 Medline

10. D. Wang, H. L. Xin, R. Hovden, H. Wang, Y. Yu, D. A. Muller, F. J. DiSalvo, H. D. Abruña, Structurally ordered intermetallic platinum-cobalt core-shell nanoparticles with enhanced activity and stability as oxygen reduction electrocatalysts. *Nat. Mater.* **12**, 81–87 (2013). doi:10.1038/nmat3458 Medline

11. J. Zhang, H. Yang, J. Fang, S. Zou, Synthesis and oxygen reduction activity of shape-controlled Pt_3Ni nanopolyhedra. *Nano Lett.* **10**, 638–644 (2010). doi:10.1021/nl903717z Medline

12. C. Cui, L. Gan, M. Heggen, S. Rudi, P. Strasser, Compositional segregation in shaped Pt alloy nanoparticles and their structural behaviour during electrocatalysis. *Nat. Mater.* **12**, 765–771 (2013). doi:10.1038/nmat3668 Medline

13. R. Subbaraman, D. Tripkovic, D. Strmcnik, K. C. Chang, M. Uchimura, A. P. Paulikas, V. Stamenkovic, N. M. Markovic, Enhancing hydrogen evolution activity in water splitting by tailoring Li^+-$Ni(OH)_2$-Pt interfaces. *Science* **334**, 1256–1260 (2011). doi:10.1126/science.1211934 Medline

14. Y. Liu, D. Gokcen, U. Bertocci, T. P. Moffat, Self-terminating growth of platinum films by electrochemical deposition. *Science* **338**, 1327–1330 (2012). doi:10.1126/science.1228925 Medline

15. Y. Kang, M. Li, Y. Cai, M. Cargnello, R. E. Diaz, T. R. Gordon, N. L. Wieder, R. R. Adzic, R. J. Gorte, E. A. Stach, C. B. Murray, Heterogeneous catalysts need not be so "heterogeneous": Monodisperse Pt nanocrystals by combining shape-controlled synthesis and purification by colloidal recrystallization. *J. Am. Chem. Soc.* **135**, 2741–2747 (2013). doi:10.1021/ja3116839 Medline

16. M. Cargnello, V. V. Doan-Nguyen, T. R. Gordon, R. E. Diaz, E. A. Stach, R. J. Gorte, P. Fornasiero, C. B. Murray, Control of metal nanocrystal size reveals metal-support interface role for ceria catalysts. *Science* **341**, 771–773 (2013). doi:10.1126/science.1240148 Medline

17. L. Tang, B. Han, K. Persson, C. Friesen, T. He, K. Sieradzki, G. Ceder, Electrochemical stability of nanometer-scale Pt particles in acidic environments. *J. Am. Chem. Soc.* **132**, 596–600 (2010). doi:10.1021/ja9071496 Medline

18. Y. Yin, R. M. Rioux, C. K. Erdonmez, S. Hughes, G. A. Somorjai, A. P. Alivisatos, Formation of hollow nanocrystals through the nanoscale Kirkendall effect. *Science* **304**, 711–714 (2004). doi:10.1126/science.1096566 Medline

19. J. E. Macdonald, M. Bar Sadan, L. Houben, I. Popov, U. Banin, Hybrid nanoscale inorganic cages. *Nat. Mater.* **9**, 810–815 (2010). doi:10.1038/nmat2848 Medline

20. S. E. Skrabalak, J. Chen, Y. Sun, X. Lu, L. Au, C. M. Cobley, Y. Xia, Gold nanocages: Synthesis, properties, and applications. *Acc. Chem. Res.* **41**, 1587–1595 (2008). doi:10.1021/ar800018v Medline

21. M. McEachran, D. Keogh, B. Pietrobon, N. Cathcart, I. Gourevich, N. Coombs, V. Kitaev, Ultrathin gold nanoframes through surfactant-free templating of faceted pentagonal silver nanoparticles. *J. Am. Chem. Soc.* **133**, 8066–8069 (2011). doi:10.1021/ja111642d Medline

22. J. X. Wang, C. Ma, Y. Choi, D. Su, Y. Zhu, P. Liu, R. Si, M. B. Vukmirovic, Y. Zhang, R. R. Adzic, Kirkendall effect and lattice contraction in nanocatalysts: A new strategy to enhance sustainable activity. *J. Am. Chem. Soc.* **133**, 13551–13557 (2011). doi:10.1021/ja204518x Medline

23. M. E. Davis, Ordered porous materials for emerging applications. *Nature* **417**, 813–821 (2002). doi:10.1038/nature00785 Medline

24. S. A. Johnson, P. J. Ollivier, T. E. Mallouk, Ordered mesoporous polymers of tunable pore size from colloidal silica templates. *Science* **283**, 963–965 (1999). doi:10.1126/science.283.5404.963 Medline

25. M. S. Yavuz, Y. Cheng, J. Chen, C. M. Cobley, Q. Zhang, M. Rycenga, J. Xie, C. Kim, K. H. Song, A. G. Schwartz, L. V. Wang, Y. Xia, Gold nanocages covered by smart polymers for controlled release with near-infrared light. *Nat. Mater.* **8**, 935–939 (2009). doi:10.1038/nmat2564 Medline

26. M. A. Mahmoud, W. Qian, M. A. El-Sayed, Following charge separation on the nanoscale in Cu_2O-Au nanoframe hollow nanoparticles. *Nano Lett.* **11**, 3285–3289 (2011). doi:10.1021/nl201642r Medline

27. M. H. Oh, T. Yu, S. H. Yu, B. Lim, K. T. Ko, M. G. Willinger, D. H. Seo, B. H. Kim, M. G. Cho, J. H. Park, K. Kang, Y. E. Sung, N. Pinna, T. Hyeon, Galvanic replacement reactions in metal oxide nanocrystals. *Science* **340**, 964–968 (2013). doi:10.1126/science.1234751 Medline

28. D. Wang, Y. Li, Effective octadecylamine system for nanocrystal synthesis. *Inorg. Chem.* **50**, 5196–5202 (2011). doi:10.1021/ic200485v Medline

29. C. E. Dahmani, M. C. Cadeville, J. M. Sanchez, J. L. Morán-López, Ni-Pt phase diagram: Experiment and theory. *Phys. Rev. Lett.* **55**, 1208–1211 (1985). doi:10.1103/PhysRevLett.55.1208 Medline

30. F. Tao, M. E. Grass, Y. Zhang, D. R. Butcher, J. R. Renzas, Z. Liu, J. Y. Chung, B. S. Mun, M. Salmeron, G. A. Somorjai, Reaction-driven restructuring of Rh-Pd and Pt-Pd core-shell nanoparticles. *Science* **322**, 932–934 (2008). doi:10.1126/science.1164170 Medline

31. B. Hammer, L. B. Hansen, J. K. Norskov, Improved adsorption energetics within density-functional theory using revised Perdew-Burke-Ernzerhof functionals. *Phys. Rev. B* **59**, 7413–7421 (1999). doi:10.1103/PhysRevB.59.7413

32. J. Greeley, J. K. Nørskov, M. Mavrikakis, Electronic structure and catalysis on metal surfaces. *Annu. Rev. Phys. Chem.* **53**, 319–348 (2002). doi:10.1146/annurev.physchem.53.100301.131630 Medline

33. D. J. Chadi, M. L. Cohen, Special points in the Brillouin zone. *Phys. Rev. B* **8**, 5747–5753 (1973). doi:10.1103/PhysRevB.8.5747

34. D. Vanderbilt, Soft self-consistent pseudopotentials in a generalized eigenvalue formalism. *Phys. Rev. B* **41**, 7892–7895 (1990). doi:10.1103/PhysRevB.41.7892 Medline

35. J. P. Perdew, J. A. Chevary, S. H. Vosko, K. A. Jackson, M. R. Pederson, D. J. Singh, C. Fiolhais, Atoms, molecules, solids, and surfaces: Applications of the generalized gradient approximation for exchange and correlation. *Phys. Rev. B* **46**, 6671–6687 (1992). doi:10.1103/PhysRevB.46.6671 Medline

36. J. A. White, D. M. Bird, Implementation of gradient-corrected exchange-correlation potentials in Car-Parrinello total-energy calculations. *Phys. Rev. B* **50**, 4954–4957 (1994). doi:10.1103/PhysRevB.50.4954 Medline

37. J. A. Herron, J. Jiao, K. Hahn, G. Peng, R. R. Adzic, M. Mavrikakis, Oxygen reduction reaction on platinum-terminated “onion-structured” alloy catalysts. *Electrocatalysis* **3**, 192–202 (2012). doi:10.1007/s12678-012-0087-0